Anomalous temperature dependence of the effective mass in p -type Bi2Te3

V Železný, V Goian, J Navrátil, Č Drašar, M Orlita, B A Piot, J Prokleška, M Míšek, J Kaštil, S Kamba

To cite this version:

V Železný, V Goian, J Navrátil, Č Drašar, M Orlita, et al.. Anomalous temperature dependence of the effective mass in p -type Bi2Te3. Physical Review B, 2021, 104, ⟨10.1103/physrevb.104.165203⟩. ⟨hal-03750860⟩

HAL Id: hal-03750860
https://hal.science/hal-03750860v1

Submitted on 12 Aug 2022

PHYSICAL REVIEW B **104**, 165203 (2021)

Anomalous temperature dependence of the effective mass in *p*-type Bi_2Te_3

V. Železný,[1,*] V. Goian,[1] J. Navrátil,[2,3] Č. Drašar,[2] M. Orlita,[4,5] B. A. Piot,[4]
J. Prokleška,[6] M. Míšek,[3] J. Kaštil,[3] and S. Kamba[1]
[1] *Institute of Physics, Academy of Sciences of the Czech Republic, Na Slovance 2, 182 21 Prague 8, Czech Republic*
[2] *Faculty of Chemical Technology, University of Pardubice, Studentská 573, 532 10 Pardubice, Czech Republic*
[3] *Institute of Physics, Academy of Sciences of the Czech Republic, Cukrovarnická 10/112, 162 00 Prague 6, Czech Republic*
[4] *Laboratoire National des Champs Magnetiques Intenses, Université Grenoble Alpes, CNRS-UPS-INSA-EMPL, 25 rue des Martyrs, Boîte Postale 166, 38042 Grenoble Cedex 9, France*
[5] *Institute of Physics, Faculty of Mathemetics and Physics, Charles University, Ke Karlovu 5, 121 16 Prague 2, Czech Republic*
[6] *Department of Condensed Matter Physics, Faculty of Mathematics and Physics, Charles University, Ke Karlovu 5, 12116 Prague 2, Czech Republic*

(Received 2 August 2021; accepted 13 October 2021; published 25 October 2021)

Infrared reflectance measurements have been carried on highly *p*-type Bi_2Te_3 crystals over the broad temperature range from 10 to 650 K and their response function investigated. An anomalous nonmonotonous temperature dependence of the plasma edge frequency is observed—with a pronounced redshift and blueshift that appear above and below room temperature, respectively. Such behavior is explained in terms of the temperature evolution of the free carrier optical weight N/m^* given by particular temperature dependence of the total carrier concentration N (determined by transport measurements) and characteristic (optical) mass m^*. The effective mass strongly varies from $m^* = 0.1m_0$ (m_0 electron rest mass) at 10 K to $m^* = 0.5m_0$ respective $m^* = 0.9m_0$ at 650 K depending on the evaluating procedure. The interpretation is corroborated by complementary magnetotransport and magnetoreflectivity experiments.

DOI: 10.1103/PhysRevB.104.165203

I. INTRODUCTION

Bismuth telluride (Bi_2Te_3) is a layered narrow-gap semiconductor that has been extensively studied as an excellent thermoelectric material for energy conversion (Seebeck effect) and cooling applications (Peltier effect) [1–3]. Its bulk gap is sufficiently large to predestinate it as a possible candidate for spintronics applications [4].

Bi_2Te_3 has rhombohedral symmetry, space-group D^5_{3d}-$R\bar{3}m$ [5]. Its crystal structure is made of three van der Waals coupled quintuple layers stacked along the trigonal *c* axis. The layers are formed by five covalently bonded atomic layers alternating as Te(1)-Bi-Te(2)-Bi-Te(1). Because of this structure the material is strongly anisotropic and can be easily cleaved along the planes perpendicular to the trigonal *c* axis.

Since Bi_2Te_3 was shown to be a three-dimensional topological insulator [6–8], it has attracted even more interest focused on its surface properties. The surface states as the wrapped Dirac cones [9] with a linear dispersion and helical spin polarization [10,11] have been experimentally confirmed by angle-resolved photoelectron spectroscopy (ARPES) [7], Shubnikov–de Haas (SdH) oscillations [12], magnetotransport [7,9,13,14], and scanning tunneling microscopy [15].

The electronic band structure of Bi_2Te_3 is not completely understood despite a lot of work that has been performed. There is still discussion on the position and number of extremes in the conduction and valence bands. Theoretical studies based on first-principles calculation give diverse views on the band structure [16–19]. It is not even quite clear whether its gap is direct or indirect. A critical role is played by spin-orbit interaction which shifts the band extremes and changes the band profile. The resulting effect depends on its strength in comparison to orbit hybridization. Both direct and indirect natures of the energy band gap has been reported with its width varying from 0.13 to 0.23 eV in experimental studies [20,21]. ARPES studies [22–25] confirm sixfold valley degeneracy and nonparabolic dispersion in the valence band. The more recent magneto-optical experiments [26] performed on thin epitaxial layers suggest a direct band gap around 175 meV with multiple most-likely sixfold valley degeneracy.

The valence-band parameters of *p*-Bi_2Te_3 were determined using the Shubnikov–de Haas effect [27,28] and later corroborated by Köhler [29] for the of hole concentrations from 5×10^{17} to 1×10^{19} cm^{-3}. Their data show a six-valley model with ellipsoidal Fermi surfaces around the band extrema. The main axis is tilted by an angle 31.5° on the mirror plane [29]. The cyclotron effective mass for $\mathbf{B} \parallel c$ at the valence-band edge is reported $0.08m_0$ and the density-of-states effective mass of a single valley at the valence-band top $0.106m_0$. The total density-of-state effective mass at the band edge averaged over all maxima is $0.35m_0$ [29]. The cyclotron masses depend on energy indicating the nonparabolic shape of the energy band. When the Fermi energy reaches ≈20 meV for the carrier density higher than 4×10^{18} $holes/cm^3$, another

---

[*] zelezny@fzu.cz

type of valence-band states (holes) begins to be active and contributes to free carriers. Moreover, the present intrinsic point defect states seem to resonate with the valence-band maximum (VBM) states, which complicates the analysis of the VB.

Real bulk crystals of Bi_2Te_3 even nominally undoped have high carrier concentration (10^{18}–10^{19} cm^{-3}) due to self-doping by charged antisite defects with small formation energies [30,31]. As a consequence, both the transport and the optical conductivities have a distinct free-carrier contribution. It manifests itself by high DC conductivity and plasma edge in reflectivity spectrum described by the Drude model. The plasma frequency depends on sample doping [32] and temperature [20,33,34]. Surprisingly, the increase inthe plasma frequency has been observed on cooling below room temperature, whereas the free-carrier concentration (plasma frequency) usually decreases on cooling in semiconductors. A satisfactory explanation of such behavior is provided here.

In this paper, we present an infrared (IR) spectroscopic study combined with transport properties on Bi_2Te_3 single crystals. The plasma edge measured in a broad temperature range (10–650 K) shows an anomalous nonmonotonic shift. It decreases with rising temperature, passes through a minimum at room temperature, and then it increases with temperature. Combining the IR data with transport measurements such behavior is explained by the temperature dependence of optical effective mass. We also study the influence of the magnetic field on the IR properties of Bi_2Te_3. Both the magneto-optic and Shubnikov–de Haas measurements provide coherent data with the low-temperature IR reflectivity.

II. EXPERIMENT

The single crystals of Bi_2Te_3 for our experiments were synthesized from Bi and Te elements of 99.999% purity. Their stoichiometric amounts were loaded into quartz ampoules of 10-mm diameter and evacuated. The sealed ampoules were heated at 1000 K for 48 h. Then the ampoules were put at a relatively high rate of 4.5 mm/h into a region of steep temperature gradient of 80 K/cm. Single crystals of 10-mm diameter and about 60-mm long were grown using a modified vertical Bridgman method. Their orientation and crystallinity was checked by x-ray diffraction, and the crystal homogeneity was monitored by measuring the plasma edge along the ampoule axis by reflectivity. The middle parts of the selected crystals of dimensions of $10 \times 5 \times (0.1\text{–}0.2)$ and $10 \times 10 \times 1.5$ mm^3 were cut and used for our transport and IR experiments, respectively. The crystals cleave very easily perpendicularly to the trigonal axes and provide lustrous mirrorlike surfaces suitable for optical measurements.

The Hall effect and resistivity measurements were carried in a Quantum Design physical property measurement system (PPMS) and Janis/Lakeshore VPS series cryostat in the temperature ranges of 10–400 and 300–700 K, respectively. The resistivity measurements were performed by a four-point probe technique and additional contacts were fixed on the opposite sides of the sample to obtain Hall data without changing contact geometry. The current (1 mA) flowed through the sample on the (0001) plane, and the voltage drop was measured between leads (7.2-mm separation) to evaluate conductivity. The Hall voltage was measured on the (0001) plane perpendicularly to the current direction across the contacts separated 1.9 mm with magnetic fields applied along the c axis to determine the Hall coefficient and carrier concentration. The sample was transferred between the above-mentioned instruments with overlapping temperature ranges, so the data over the entire temperature range of interest were taken on the same sample keeping the identical contacts geometry.

IR reflectance was measured at near-normal incidence from the fresh crystal surface perpendicular to the c axis. No polarizer was necessary for these measurements since the electric field of the IR radiation lay on the isotropic (0001) plane normal to the trigonal c axis. The spectra were taken in the broad temperature range from 10 to 650 K and over the frequency range of 30–5000 cm^{-1} using a Bruker IFS 113v spectrometer with the spectral resolution 2 cm^{-1} and a golden-covered mirror taken as a background. For higher photon energies the reflectance measured with a PerkinElmer Lambda 1050 UV/VIS/NIR spectrometer was combined with data obtained by a visible-UV ellipsometer VASE (Woollam, Inc.) up to 70 000 cm^{-1}. The reflectance spectra were analyzed by Kramers-Kronig transforms and oscillator fits. The metallic Hagen-Rubens relation ($R \propto 1 - \sqrt{\omega}$) for low frequency and ($R \propto \omega^{-2}$) up to 10^6 cm^{-1} and a free-electron dependence ($R \propto \omega^{-4}$) for higher-frequency extrapolations were used for the Kramers-Kronig analysis and combined with the ellipsometric data. Using this procedure and spectra fitting, the complex optical conductivity $\hat{\sigma}(\omega)$ and dielectric function $\hat{\varepsilon}(\omega)$ were obtained.

Magnetoreflectance experiments were performed in a custom-made cryostat. The measurement was performed in the Faraday geometry with electromagnetic wave propagation along the c axis ($\mathbf{B} \parallel k \parallel c$) and with a magnetic field varying up to 32 T. The frequency-dependent sample reflectance was recorded and normalized by the reflection spectrum of the reference mirror for all temperatures and magnetic fields.

III. RESULTS AND DISCUSSION

The measurements of the Hall coefficient (R_H) reveal rather high hole concentration ($\sim 2.1 \times 10^{19}$ cm^{-3}) corresponding to a saturated semiconductor region even at very low temperatures. They are shown in Fig. 1(b) and are in good agreement with literature [35–37]. Such high hole concentration is most likely due to the presence of negatively charged antisite defects Bi_{Te} [38]. According to the Hall measurement, they are localized in a close vicinity of the VBM [see scheme in Fig. 1(a)] or even resonate with the VBM states. This means that the acceptors are active down to very low temperature. Although the measured DC conductivity (σ_{DC}) exhibits up to 300-K typical metallic character a detailed inspection of Hall coefficient reveals a nonmonotonic behavior; it decreases to a shallow minimum at 60 K with a subsequent increase towards 300 K as shown in Fig. 1(b). This unusual feature can be explained by the existence of two valence bands or subbands [39]. The observed depression in R_H and behavior of σ_{DC} in this temperature range indicates that the second band of heavier holes takes part in transport. The existence of the second valence band (or second type of hole with concentration p_2) is in accordance with the results of von Middendorf

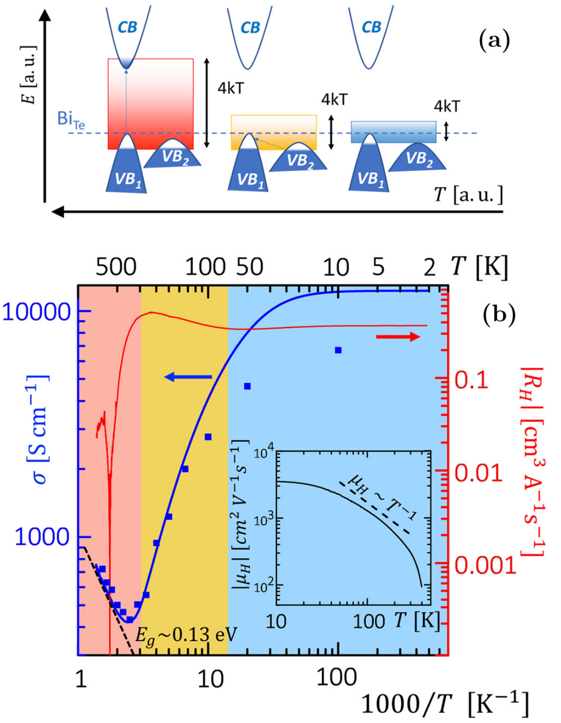

FIG. 1. (a) Energy scheme explaining the occupation of bands and their temperature dependence. (b) Temperature dependence of experimental DC conductivity and Hall coefficient (magnetic-field 1 T, solid lines). The energy gap $E_g = 0.13$ eV is determined from the plot of the total carrier concentration versus $1/T$. All quantities have logarithmic scales. The experimental DC conductivity is compared with static conductivity determined by fitting the reflectance spectra using the Drude model (solid blue symbols). The inset in panel (b) shows the temperature dependence of experimental mobility and its comparison with the fit $\mu_H \sim T^{-1}$.

and Landwehr [28], Köhler [29], and Kulbachinskii *et al.* [40], and it is hinted from our measurements of SdH oscillations presented below (Fig. 2). In the low-temperature region, below $T \sim 70$ K, the transport is associated with light holes, whereas above $T \sim 70$ K, both bands take part in charge transport. The total concentration of holes is dictated by the concentration of accessible acceptor levels and, thus, almost temperature independent. In the low-temperature region, the total hole concentration corresponds to the hole concentration of light holes $P_t = p_1$. In the high-temperature region, the total concentration of holes comprises both types of holes $P_t = p_1 + p_2$. As mentioned above, this scenario is consistent with the experiment (σ_{DC} and R_H) when $\mu_1 > \mu_2$, i.e., when $m_2 > m_1$. This is also the reason of the increase in the effective mass calculated from infrared data in this temperature region.

A high degree of degeneracy and the presence of two types of holes gives rise to a distinct temperature dependence of Hall mobility (see the inset in Fig. 1). The temperature dependence is typical for quasidegenerate semiconductors (Si, Ge [41], and Bi_2Te_3 [42]) when a combination of scattering on ionized impurities and acoustic phonons is considered.

The semiconducting behavior of the measured sample above 400 K is connected with intrinsic excitations of electrons over the band gap. This is corroborated by the Hall coefficient which drops rapidly and changes the sign at $T \geqslant 530$ K. We used the same evaluating procedure as Shigetomi and Mori and Jeon *et al.* [35,36]. They have studied the stoichiometric *p*-type Bi_2Te_3 of very similar parameters (both σ_{DC} and R_H, and their temperature dependence) and have shown that the ratio $m_e m_h / m_0^2 \sim 1.35$ is obtained when modeling this temperature region using the experimental data. This is in accordance with a high-temperature effective mass calculated from optical data as discussed below (Fig. 9).

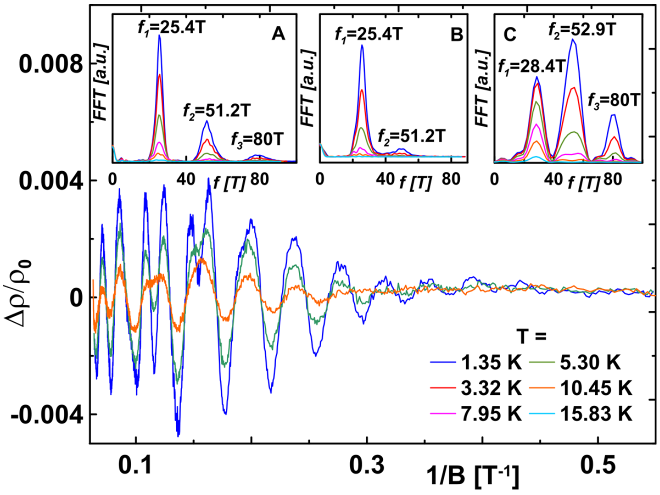

FIG. 2. The Shubnikov–de Haas magnetoresistance oscillations at several temperatures. Panels (a)–(c) show fast Fourier transformation (FFT) curves obtained from the SdH oscillations for the field range (a) from 1.5 to 15.5 T, (b) 1.5 to 6 T, and (c) 6 to 15.5 T.

We note that our experimental values of DC conductivity are always higher than those calculated from the IR spectra as shown in Fig. 1. This trend is enhanced on cooling, which suggests existence of another low-frequency dispersion below the IR region.

We measured the SdH effect with the aim to confront the effective mass and concentration of carrier obtained from IR spectroscopy. Pronounced SdH magnetoresistance oscillations ($B = 2$–15 T) were observed (Fig. 2) at low temperatures ($T = 1.5$–20 K). Fourier transform of the full SdH data revealed three distinct peaks [inset (a) in Fig. 2]. The main peak at frequency ($f_1 = 25.4$ T) and its harmonics ($f_2 = 51.2$ T) can be attributed to light holes of the upper valence band (UVB) and its spin splitting, respectively, which is in accordance with Köhler [29]. The weak peak at $f_3 = 80$ T can be attributed to heavy holes of the lower valence band (LVB) previously envisaged by Middendorf and Landwehr [28], Köhler [29], and Kulbachinskii *et al.* [40]. Based on the present data, we estimated the concentration of light and heavy holes considering the six-ellipsoid Drabble-Wolfe model [43] and using the inverse effective mass tensor α_{ij} as calculated by Köhler [44]. Generally, the *i*th SdH frequency can be related to the concentration of holes p_i [45,46],

$$f_i(B) = \frac{\hbar(3\pi^2 p_i/K_e)\sqrt[3]{\alpha_{11}\left(\alpha_{22}\alpha_{33} - \alpha_{23}^2\right)}}{2e\sqrt{\alpha_{11}\alpha_{22}}}, \tag{1}$$

where $\hbar$ is the reduced Planck constant and K_e is the number of ellipsoids within the first Brillouin zone. Although the

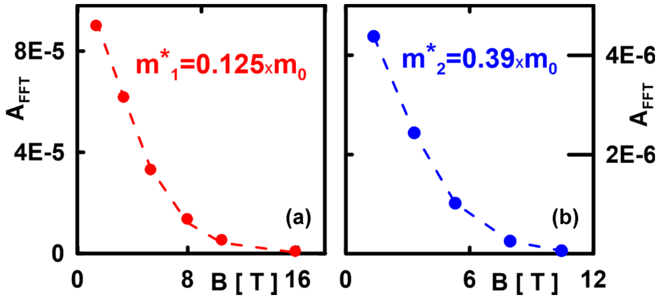

FIG. 3. Field dependence of FFT amplitudes of the 25.4-T peak, i.e., (a) for light holes and (b) of the 80-T peak, i.e. heavy holes.

procedure is well applicable to UVB, its use for LVB is disputable. The band parameters of LVB are unknown (nonparabolicity, effective-mass tensors). Thus, the data for LVB must be considered as a first approximation. Using (1), we obtained $p_1 = 3 \times 10^{18}$ cm^{-3} (UVB light holes) and $p_2 = 1.6 \times 10^{19}$ cm^{-3} (LVB, heavy holes) at 2 K. The sum of the hole concentrations $p_{\mathrm{SdH}} = p_1 + p_2 = 1.9 \times 10^{19}$ cm^{-3} calculated from the SdH oscillations then corresponds well to the concentration found from the Hall coefficient measurements as $p_{R_H} = 1/(R_H e) = 2.1 \times 10^{19}$ cm^{-3}.

The data analysis was as follows. First, we analyzed SdH oscillations at a low magnetic fields where spin splitting is negligible to obtain the effective mass of UVB holes m_1^* using the Lifshitz-Kosevich fit of the temperature-dependent normalized amplitudes of magnetoresistance oscillations (Fig. 2) in the field range of $B = 3$–5 T. We obtained the average mass of $m_1^* = 0.12 \pm 0.01 m_0$ a value well comparable with literature [29]. We obtain almost the same cyclotron mass $m_1^* \cong 0.125 m_0$ [Fig. 3(a)] using this fit to temperature-dependent amplitudes of Fourier transforms for the low-field range [Fig. 2(b)] [47]. Thus, the temperature-dependent amplitudes of Fourier transforms are applicable for this analysis. To better resolve the presence of heavy holes we performed FT analysis of high-field oscillations separately [Fig. 2(c)]. For the heavy holes ($f_3 = 80$ T) we obtained $m_2^* \cong 0.39 m_0$ [Fig. 3(b)]. Although the m_2^* value is very approximate it matches well the DFT calculations of Chen *et al.* [7] showing the LVB edge a couple of meV below the UVB edge. Due to strong nonparabolicity [29] the mass is strongly dependent on the position of the Fermi level, and it is even more energy dependent for more degenerate samples. The Fermi level (with respect to the band edge) can be estimated using Schröder *et al.* [48],

$$E_F = \frac{\hbar^2}{2m_1^*}\left(3\pi^2 \frac{p_1}{K_e}\right)^{2/3}. \tag{2}$$

This relation applies to the six-ellipsoid model with the parabolic dispersion, and, hence, it is applicable to UVB giving Fermi energy $E_F = 18$ meV which is consistent with values published previously [29]. Although its application to strongly nonparabolic bands is more than disputable, we obtained a reasonable value of $E_F = 19$ meV for LVB, which qualitatively corresponds to the DFT picture by Chen *et al.* [7]. Note that the actual concentration of native defects may play an important role due to mixing of defect states with VBM states.

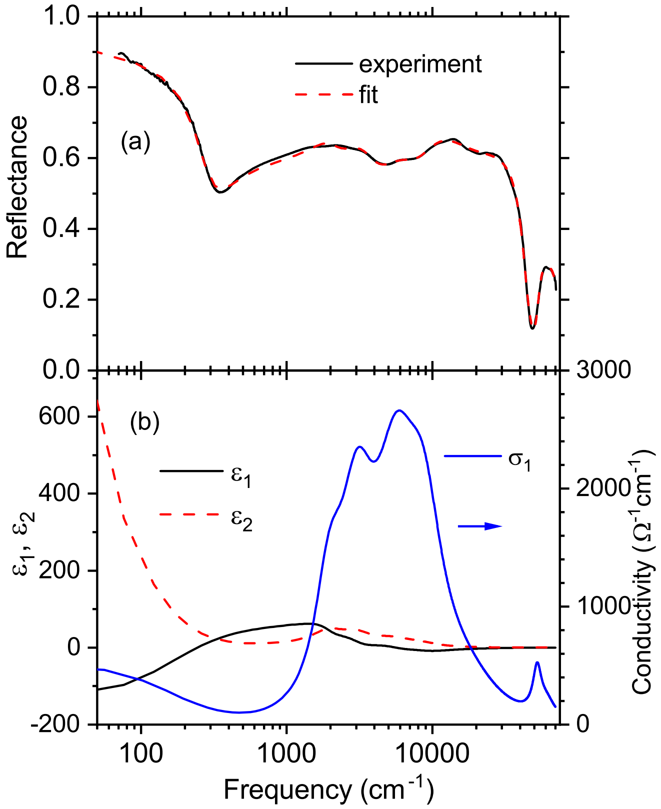

FIG. 4. (a) Room-temperature reflectance and its fit over the entire spectral range on a logarithmic scale. (b) Calculated complex dielectric function $\hat{\varepsilon} = \varepsilon_1 + i\varepsilon_2$ and the real part of optical conductivity $\sigma_1 = \nu\varepsilon_2/60$, where ν is in cm^{-1} and σ_1 is in Ω^{-1} cm^{-1}.

Near-normal reflectance at room temperature with the electric-field polarization in the plane perpendicular to the crystal *c* axis over very broad frequency range from 30 cm^{-1} to 70 000 cm^{-1} on a logarithmic scale is shown in Fig. 4(a). The displayed curve is obtained combining the experimental IR and optical reflectance with the reflectivity calculated from the spectroscopic ellipsometry.

The spectrum in the IR range displays a typical metallic character. The high $R(\omega)$ value quickly drops down to a minimum approximately at 400 cm^{-1} in a way known as a plasma edge that is caused by the presence of free carriers. The additional spectral features clearly visible at higher energies are caused by interband electronic transitions. The modeling of the reflectivity spectrum in Fig. 4 provides also other optical response functions as the complex optical conductivity and dielectric function.

In order to determine the parameters of individual spectral features and to obtain a deeper insight in the electronic properties of Bi_2Te_3, we analyze the spectra using a simple Drude-Lorentz model. The normal specular reflectance for a thick (opaque) sample is expressed by normal reflectivity $R(\omega)$,

$$R(\omega) = \left|\frac{\sqrt{\hat{\varepsilon}(\omega)} - 1}{\sqrt{\hat{\varepsilon}(\omega)} + 1}\right|^2. \tag{3}$$

TABLE I. The parameters of the Lorentz oscillators obtained by fitting the room-temperature reflectance spectrum.

j	ω_j (cm^{-1})	$\omega_{p,j}$ (cm^{-1})	γ_j (cm^{-1})
1	1960	7750	1100
2	3050	13490	2050
3	5610	21780	4620
4	8740	22730	6440
5	17090	19130	21950
6	52390	13880	8590
7	61040	12280	19180

The complex dielectric function $\hat{\varepsilon}(\omega)$ is given

$$\begin{aligned}\hat{\varepsilon}(\omega) &= \varepsilon_1(\omega) + i\varepsilon_2(\omega)\\ &= \varepsilon_\infty - \frac{\Omega_p^2}{\omega^2 + i\gamma\omega} + \sum_{j=1}^{n} \frac{\omega_{p,j}^2}{\omega_j^2 - \omega^2 - i\omega\gamma_j},\end{aligned} \quad (4)$$

where ε_∞ reflects high-energy contributions to the dielectric function from the excitations above the measured interval, the second term describes the free-carrier (so-called Drude) contribution (Ω_p is the plasma frequency, and γ is the damping), and the last term expresses the sum of contributions from optical active excitations. The ω_j, γ_j, and $\omega_{p,j}$ are their resonance frequency, damping, and oscillator strength, respectively.

Figure 4(a) shows that the experimental reflectance is reasonable well fit by our simple model [Eqs. (3) and (4)] consisting of one Drude term and seven harmonic oscillators representing interband electronic transitions. The spectra are computed using REFFIT software [49]. The oscillators' parameters determined by the fitting procedure are given in Table I where the first oscillator roughly simulates the optical band gap. The calculated functions $\varepsilon_1(\omega)$, $\varepsilon_2(\omega)$, and $\sigma_1(\omega)$ are displayed in Fig. 4(b). The $\varepsilon_1(\omega)$ shows negative values, and the $\varepsilon_2(\omega)$ diverges at low frequencies as typical for materials containing free carriers. The progressive rise in $\sigma_1(\omega)$ and $\varepsilon_2(\omega)$ above ($E_g \simeq$ 1200 cm^{-1}) (150 meV) corresponds well to the expected onset of interband absorption. The band gap is in good agreement with the value given in literature [20,21,26]. Much detailed analysis has been performed up to 6 eV (48 000 cm^{-1}) by Dubroka *et al.* [21]. Their wider band gap is a consequence of the Moss-Burstein shift (Pauli blocking) [43]. The lower value of our band gap is a result of high doping when the dopants (native defects) begin to form an impurity band that leads to smearing of the band-gap edge.

As the most interesting changes in our spectra are observed in the far-IR region we focused on them. The temperature dependence of the spectra is displayed in Figs. 5(a) and 5(b) for the low- and high-temperature range, respectively. All these spectra show a typical metallic response dominated by a well-developed plasma edge localized close to the reflectance minimum. Although the selection rules allow the observation of IR-active phonons, they are not observed in our spectra because their oscillator strength is completely screened out by the high concentration of free carriers. Other authors [50] reporting on the phonon observation had less conducting samples. In the low-temperature spectra [Fig. 5(a)], it is seen as a strong decrease in the plasma edge with increasing temperature. The plasma edge at 440 cm^{-1} at 10 K drops down to its minimum position at 280 cm^{-1} at room temperature. Above room temperature, there is, on the contrary, a monotonous increase in the plasma frequency with temperature, and it reaches the value of 470 cm^{-1} at 650 K as illustrated in Fig. 5(b).

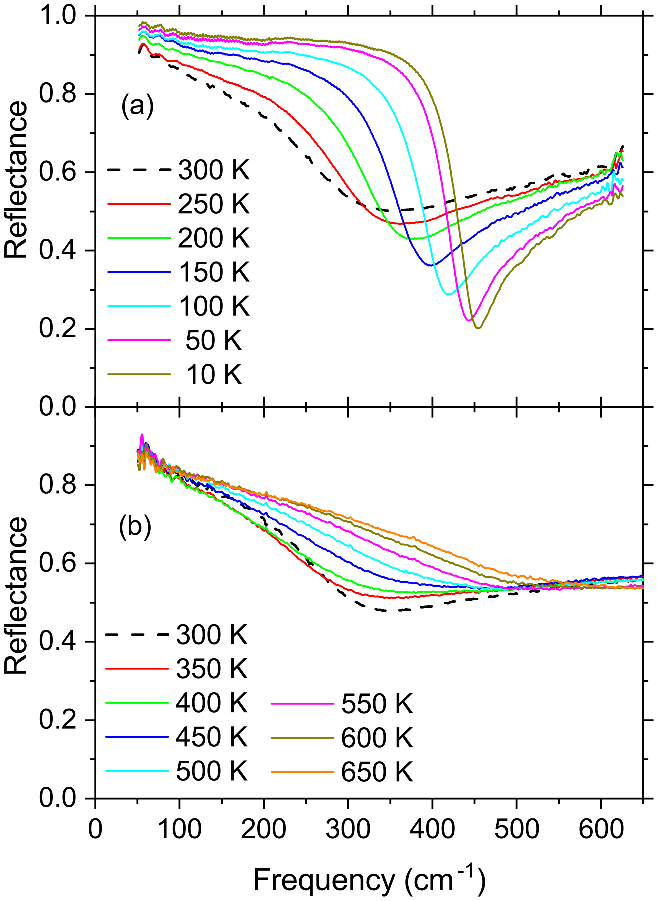

FIG. 5. Temperature dependence of far-IR reflectance: (a) below room temperature and (b) above it.

The temperature dependence of the plasma parameters (plasma frequency and damping) provides important information about free-carrier dynamics. They are determined by fitting the experimental IR reflectance given in Fig. 5. For fitting the IR spectra we again use that Eqs. (3) and (4), but in Eq. (4) we limit ourselves to the first two terms. In this case, a new ε_∞^{IR} is also introduced which includes the contributions of all electronic interband transitions obtained from the third term of Eq. (4) and the original ε_∞. The plasma frequency obtained by this fitting procedure corresponds to unscreened plasma. The unscreened plasma frequency Ω_p is sometimes also called spectral weight because according to the sum rule it is defined as an integral of $\sigma_1(\omega)$ over the entire frequency range and is related to the total charge density. The damping parameter $\gamma = 1/\tau$ is related to the carrier life time τ and characterizes charge-carrier scattering processes.

An additional illustration of the plasma behavior is presented in Fig. 6 where the temperature dependence of the

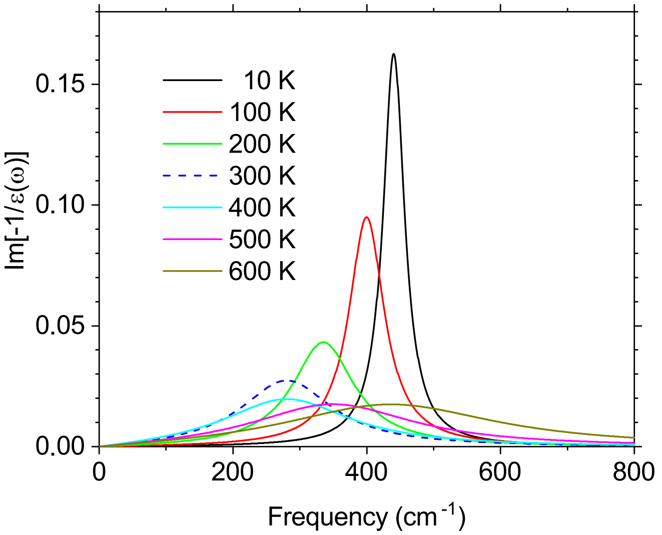

FIG. 6. Temperature dependence of the energy-loss function for selected temperatures. Its maximum corresponds to screened plasma edge Ω_p^*.

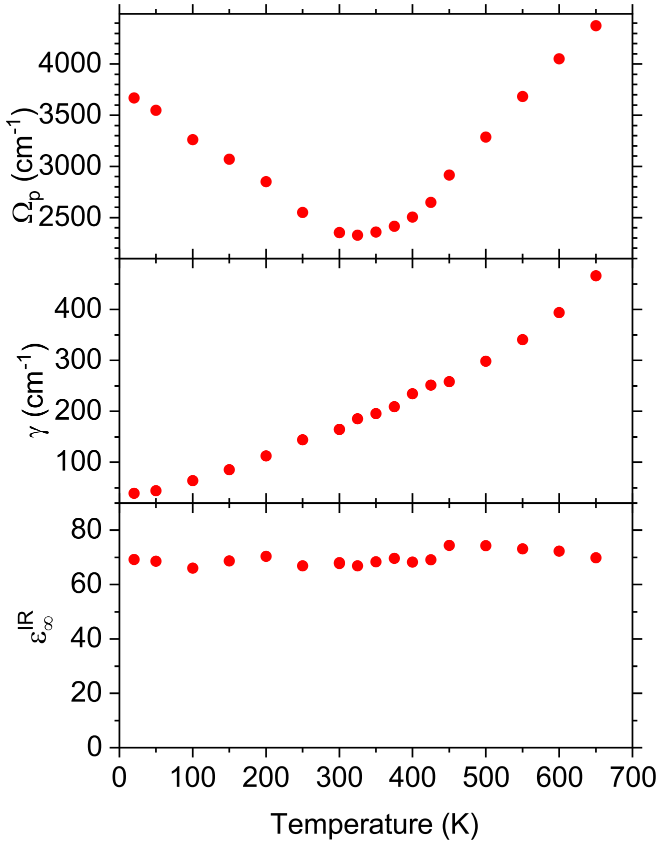

FIG. 7. Temperature dependence of the parameters of the Drude model Ω_p, γ, and ε_∞^{IR} obtained by fitting the far IR reflectance.

energy-loss function $\mathrm{Im}[-1/\hat{\varepsilon}(\omega)]$ is shown. Its maximum corresponds to the screened plasma frequency Ω_p^* defined as the zero of the dielectric function. It is located close to plasma edge, and it is related to the screened one by the formula $\Omega_p^* = \Omega_p/\sqrt{\varepsilon_\infty^{IR}}$. The peak position in $\mathrm{Im}[-1/\hat{\varepsilon}(\omega)]$ reaches the minimal frequency near 300 K, and then it increases independently of either temperature increases or temperature decreases. The width of the energy-loss function is linked to the carrier damping γ. It is growing in the entire temperature range. Another fact that illustrates a complex behavior of this material is the temperature dependence of DC conductivity calculated from the parameters determined by the fitting procedure. Below 300 K, its value is lower than the experimental DC values as shown and discussed in Fig. 1.

The plasma parameters in Fig. 7 extracted from our fit illustrate very clearly their nontrivial temperature behavior. The most remarkable and anomalous behavior shows the unscreened plasma frequency Ω_p in Fig. 7(a). It is decreasing on heating from 3700 cm^{-1}, reaches a minimum of 2300 cm^{-1} at room temperature, and then this trend is reversed and the plasma frequency begins to grow and reaches the value of 4300 cm^{-1} at 650 K.

The plasma damping in Fig. 7(b) shows a monotonous and practically linear increase in the entire temperature interval. Its large variation (from 30 cm^{-1} at 10 K to 470 cm^{-1} at 650 K) indicates that a strong electron-phonon interaction or a complex band structure is responsible for this effect.

Figure 7(c) shows the temperature dependence of the new $\varepsilon_\infty^{IR} \approx 70$ that includes the contributions of all electronic transitions up to 70 000 cm^{-1} plus the original ε_∞^{IR}. The ε_∞^{IR} is constant in the whole measured temperature interval within the accuracy of our fit. Its value is in good agreement with ε_1 at 700 cm^{-1} in Fig. 4 where the fit of the entire broad spectrum has been performed. The temperature independence of ε_∞^{IR} is important evidence that the shift of the plasma frequency is not influenced by the high-frequency interband transitions but is caused only by the variation of the parameters of the free-carrier plasma.

The application of magnetic-field results in additional effects in the IR spectra that can be used for effective mass determination. The reflectance measured at 1.8 K using nonpolarized radiation in the Faraday geometry (i.e., with B applied parallel with wave vector of radiation) in the magnetic fields up to 32 T is displayed in Fig. 8 in a form of magnetoreflectivity R_B and relative change in reflectivity R_B/R_0 in the lower and upper panels, respectively. The magnetic field, applied along the c axis of the crystal, leads to a clear splitting of the plasma edge. According to the classical magnetoplasma theory [51], the position of the plasma edge depends on the sense of circular polarization of the probing radiation. In the limit of vanishing dissipation, the plasma edge is theoretically expected at the energy of $\omega_c/2 + \sqrt{\omega_c^2/4 + \omega_p^2}$ and $-\omega_c/2 + \sqrt{\omega_c^2/4 + \omega_p^2}$ for so-called cyclotron resonance active (CRA) and cyclotron resonance inactive (CRI) modes, respectively. This allows us to get, in principle, a solid estimate of the cyclotron energy ω_c and, consequently, of the effective cyclotron mass ($\omega_c = eB/m_{\mathrm{CR}}$). In our experimental case, with a non-negligible and B-dependent dissipation and the response measured using nonpolarized radiation, the precise readout of the plasma edge position becomes a more complex task. Nevertheless, one can still roughly estimate the cyclotron energy from the relative distance of the CRA and CRI plasma edges

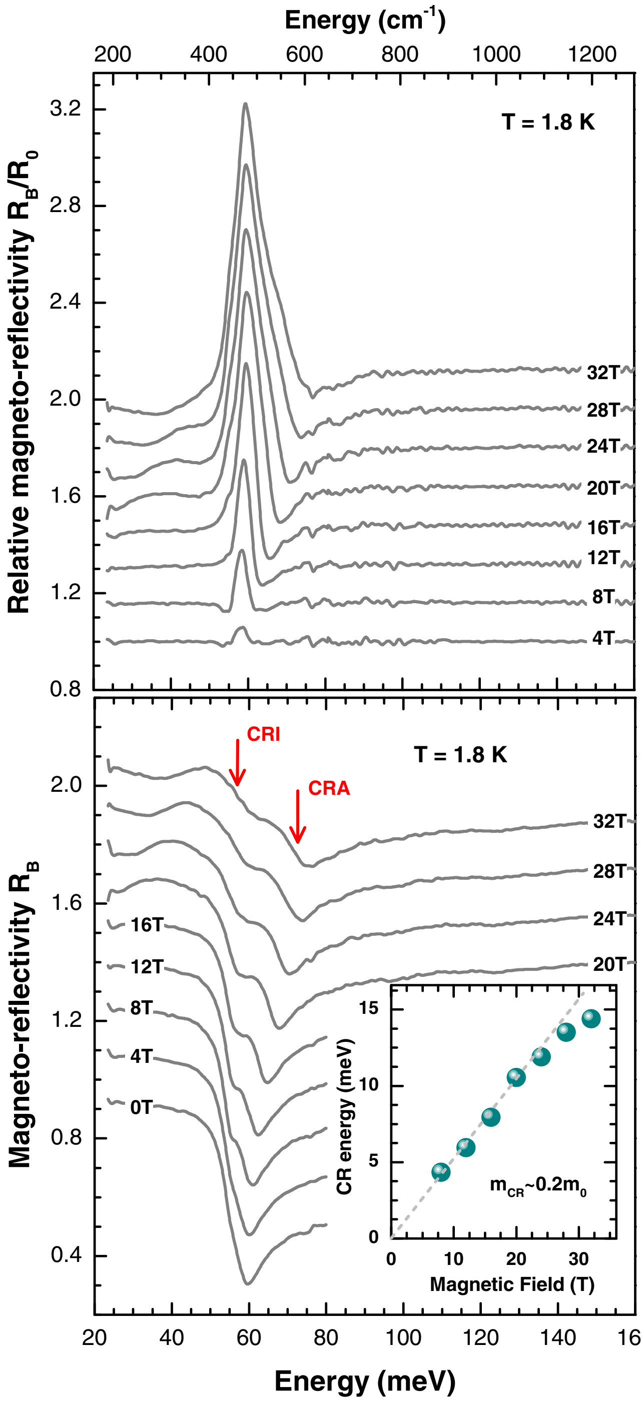

FIG. 8. Lower panel: Dependence of IR reflectance on the applied magnetic-field R_B measured at 1.8 K. The inset shows the dependence of the deduced cyclotron energy on B. Upper panel: Relative change in infrared reflectivity with the magnetic-field R_B/R_0.

which are manifested in our data by the steplike profile of R_B observed in high magnetic fields. In detail, we have deduced the cyclotron energy (see the inset in the lower panel of Fig. 8) as a separation of the corresponding inflection points (red vertical arrows in the lower panel of Fig. 8). Interestingly, the cyclotron energy deduced in this way flattens in high magnetic fields. Such behavior may suggest the impact of nonparabolicity of the band, implying an increase in the effective mass with the energy (or momentum). At the same time, in high magnetic fields, we necessarily approach the quantum regime of the studied material which limits the validity of the classical magnetoplasma theory. Therefore, to estimate the effective mass, we have only relied on the magnetoreflectivity data collected at relatively low fields (below 25 T) where the cyclotron energy is, within the experimental precision, a linear function of B (dashed line in the inset of Fig. 8). Our estimate of the cyclotron mass $m_{\mathrm{CR}} = 0.2$ is slightly higher, nevertheless, still comparable with the effective mass deduced from the plasma frequency itself (Fig. 9) and from the magnetotransport data.

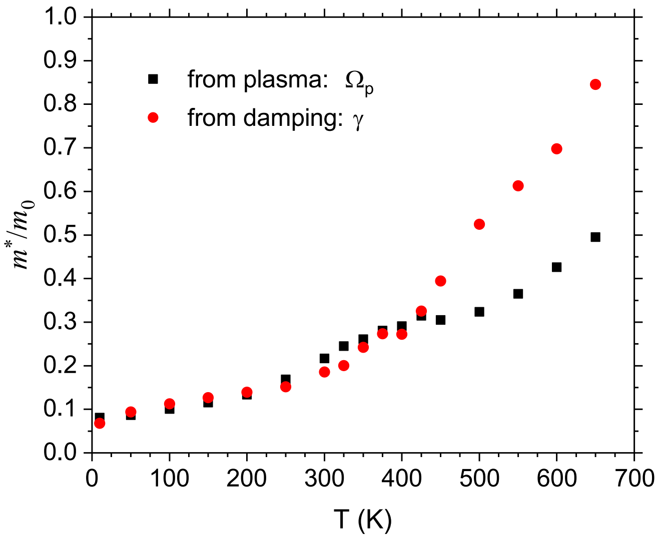

FIG. 9. Temperature dependence of the relative optical effective mass of charge carriers calculated from the plasma frequency and its damping.

The Drude theory links the plasma frequency Ω_p to the carrier concentration n and the effective mass m^* by $\Omega_p^2 = 4\pi ne^2/m^*$ and similarly the mobility μ is related to the scattering time τ and effective mass by $\mu = e\tau/m^*$. Both Ω_p and μ now represent effective quantities that involve the contributions of several types of carriers and are temperature dependent. Their total concentration is $n_{\mathrm{tot}} = n_i + p_i + P_t$, where n_i and p_i are the concentrations of intrinsic electrons and holes which are generated only above room temperature and $P_t = p_1 + p_2$ is the extrinsic concentration defined above in the transport part. Determining independently the transport quantities (n and μ) and combining them with the plasma parameters (Ω_p and γ) provides a way how to determine the so-called optical mass. It can be generally different from the effective mass determined by other techniques, such as cyclotron resonance, SdH experiments, or theoretical calculation. We tried to fit the IR reflectance a model involving the different carriers to distinguish and single out their contributions, but we failed because the fits were not stable.

The temperature dependence of the effective mass evaluated from Ω_p is displayed in Fig. 9. It shows a slow and monotonous variation from the value of $0.1m_0$ at low temperatures to the value of $0.2m_0$ at room temperature. Above 400 K its value starts to grow slightly faster, and it reaches the value of $0.5m_0$ at 650 K. The heavier effective mass is caused by additional carriers thermally generated across the band gap.

Fitting the IR reflectivity provides another parameter γ that can be used to determine effective mass. To get effective mass the expression for the total carrier mobility $z\mu_{\mathrm{tot}}(T) = e\tau_{\mathrm{tot}}(T)/m^*_{\mathrm{tot}}(T) = \sigma_{\mathrm{tot}}(T)/[en(T)]$ is used where all quantities are again temperature dependent. The quantities with the subscript tot involve contributions from all the types of carriers taking part in the transport properties [35,36]. The scattering time in seconds, $\tau_{\mathrm{tot}} = 1/2\pi c\gamma$ (if γ is in cm^{-1} and c is the light velocity), is identified with plasma damping obtained from the fit of the IR spectra. The temperature dependence of the effective mass obtained in this way has a very similar run to that determined from the plasma frequency below room temperature as is demonstrated in Fig. 9. At higher temperature they start to differ. Their deviation can be explained that the plasma frequency is determined by the charge concentration of (mixing of CBM electrons and VBM holes) whereas the damping reflects carrier scattering processes.

From the above-presented data, we can see that the most striking effect is the substantial change in the plasma frequency of $\mathrm{Bi_2Te_3}$ with temperature and the related change in the optical effective mass. The values of the effective mass obtained by the IR measurement is in good agreement with our data obtained by other techniques (magneto-optics and SdH effect) at low temperatures and with the data previously obtained by other investigators.

The fundamental parameters of semiconductors (energy gap and effective mass) depend on temperature. Theoretical models [52–54] explain it by lattice dilatation and electron-phonon interaction. Experimental investigations mention very small variation of effective mass with temperature in classical semiconductors [55]. Much larger variation (of 50%) is reported for PbTe [56]. This change is too large to be explained in the framework of the $\mathbf{k} \cdot \mathbf{p}$ perturbation method that uses as the parameter tensor characters of effective mass and nonparabolic dispersion of bands. In the case of $\mathrm{Bi_2Te_3}$ the change in the effective mass is much larger, and its explanation must be found beyond any of these theories.

To understand the strong temperature dependence of effective mass the complex structure of the $\mathrm{Bi_2Te_3}$ electronic bands has to be taken into account. Theoretical first-principles study [16,17] including strong spin-orbit interaction results in small band gaps, nonparabolic, and linear band, and small effective mass and high valley degeneracy that have been experimentally observed using ARPES [7]. A conflicting points remain the positions and degeneracy of the band extrema [19,26, 57–59]. The crystal symmetry places them on the bisectrix (mirror plane) of the Brillouin zone which leads to sixfold degenerate Fermi-surface pockets. The calculations [60,61] also predict two types of nonparabolic hole pockets (light and heavy holes). With increasing doping the Fermi surface becomes more complex, the pockets elongate, and finally they link together forming a ring structure having a corrugated character [7,57]. The theoretical predictions are in good agreement with the experimental data and models used for the interpretation of magnetoquantum investigations [27–29].

Let us now present a scenario that relates together the transport and infrared data and interprets the above-described effects. We need for it a quite complex model consisting of two valence bands (light and heavy holes—see Fig. 1), conduction band, and acceptor level located very close to the valence band. The model is also based on the theoretical and experimental results from literature presented above. At low temperatures, $\mathrm{Bi_2Te_3}$ is a p-type extrinsic semiconductor. The light holes with effective mass of $0.1m_0$ are excited into the valence band at its edge from the antisite defect level and are responsible for the high plasma frequency of $3700\ \mathrm{cm}^{-1}$. As temperature rises the hole concentration increases only very slightly as indicated by the Hall data. At the same time the deeper states with heavier m^* corresponding to the second valence-band level start to be occupied with heavy holes. As their dispersion is flatter than the light holes they have higher density and their contribution increases with increasing temperature. This implies that the averaged effective mass increases, the plasma frequency decreases on with rising temperature and reaches its minimum at room temperature where it is equal to $2300\ \mathrm{cm}^{-1}$.

Above room temperature the excitations across the band gap begin to take place, and the intrinsic concentration of electron-hole pairs starts exponentially to grow and causes the increase in the plasma frequency. $\mathrm{Bi_2Te_3}$ passes to the intrinsic regime. The Hall coefficient sharply drops and at 530 K crosses zero and changes its sign which is a typical feature demonstrating a extrinsic to intrinsic regime crossover. The growth of carrier concentration on one hand leads to the increase in the effective mass due to the nonparabolicity of the valence band and the shift of the Fermi level—on the other hand the exponential growth of the carrier concentration prevails, and the plasma frequency grows, and at 650 K reaches the value of $4300\ \mathrm{cm}^{-1}$. The complex temperature dependence of the plasma frequency and effective mass observed in our experiments is explained by the competition between the complex band structure of $\mathrm{Bi_2Te_3}$ and a transition between different regimes of generating carriers depending on temperature.

The higher values of the effective mass obtained from the mobility data above room temperature are caused by the sensitivity of the mobility to scattering mechanisms which appear due to increasing concentration of carriers.

The layered crystal structure of $\mathrm{Bi_2Te_3}$ and the weakness of the van der Waals Te(1) - Te(1) bonds between the adjacent quintuples suggests another interpretation of the temperature behavior of the effective mass. The thickness of a quintuple layer is ≈ 3 nm what is similar to the thickness of two-dimensional electron gas (2DEG) in metal-oxide-semiconductor field-effect transistor (MOSFET) transistors. Its behavior has been recently studied combining terahertz optical Hall-effect measurements with IR spectroscopic ellipsometry. It has been found in AlGaN/GaN high electron mobility transistor structures [62] that the effective mass increases from $0.22m_0$ at 1.5 K to $0.36m_0$ at 300 K. Simultaneously, the mobility μ falls monotonously down in this temperature interval limited at low temperatures by impurity scattering contribution of remote impurities, and for high temperatures it is limited by polar-optical phonon scattering. The effective-mass behavior is explained by the reduction of the 2DEG confinement, i.e., the wave function penetrates from the AlGaN with increasing temperature. Similar unusual behavior of effective-mass temperature dependence has been already theoretically predicted in several cases connected with 2DEG

[63]. Thus, the results may alternatively suggest a transition from 2D to three-dimensional character of carrier behavior.

The behavior reminiscent of topological insulators has been observed in InAs/GaSb quantum wells. In all the cases including our one, a common factor is the large anisotropy approaching two dimensionality. It can be another cause that supports such behavior [63].

IV. CONCLUSIONS

We have studied the temperature dependence of the reflectance and transport properties in *p*-type Bi_2Te_3 single crystals, a thermoelectric material that is currently also very intensively studied for its topological insulator behavior. The unusual temperature dependence of the plasma frequency was observed in the IR spectra that unlike in classical semiconductors, decreases on heating from 10 to 300 K having the minimum at room temperature and then again increases above room temperature whereas its damping is monotonously increasing. The charge-carrier concentration extracted from the Hall and conductivity measurement shows a weak variation on heating from 10 K up to room temperature and then steeply rises. The Hall coefficient at 530 K changes its sign due to the electronic transitions across the band gap, and Bi_2Te_3 passes over to intrinsic regime. Combining the IR and transport data the effective mass is determined, and it is found that it is extremely increasing (based on evaluation method 500–900%) in the entire temperature interval. The low-temperature effect is explained by the existence of two types (light and heavy) holes, and the values of the effective mass are independently confirmed by Shubnikov–de Haas effect measurement as well as by magnetooptic studied (observation of cyclotron resonances in external magnetic field). Above room temperature the strong increase in the effective mass is compensated by the exponential rise of carrier concentration due to their generation across the band gap which leads to a further increase in the plasma frequency. In addition, our experiments indicates the important role of the defect level in proximity to the VBM. It was also found an analogy in the effective-mass behavior in Bi_2Te_3 and the two-dimensional electron gas in MOSFET transistors.

ACKNOWLEDGMENTS

This work was supported by the Czech Science Foundation (Projects No. 21-06802S and No. 19-16315S), by the Operational Programme Research, Development and Education (financed by European Structural and Investment Funds and by the Czech Ministry of Education, Youth and Sports), by the Project No. SOLID21 (CZ.02.1.01/0.0/0.0/16|019/0000760), and by the Program of Czech Research Infrastructures (Project No. LM2018096).

---

[1] R. Sehr and L. R. Testardi, J. Appl. Phys. **34**, 2754 (1963).
[2] *MRS Symposia Proceedings, Boston, 1998*, edited by T. Tritt, M. Kanatzidis, G. Mahan, and H. Lyon (Material Research Society, Pittsburgh, 1999), Vol. 545.
[3] T. M. Tritt, Science **283**, 804 (1999).
[4] M. He, H. Sun, and Q. L. He, Front. Phys. **14**, 43401 (2019).
[5] R. Wyckoff, *Crystal Structures* (Krieger, Melbourne, FL, 1986), Vol. 2.
[6] J. Moore, Nature (London) **464**, 194 (2010).
[7] Y. L. Chen, J. G. Analytis, J.-H. Chu, Z. K. Liu, S.-K. Mo, X. L. Qi, H. J. Zhang, D. H. Lu, X. Dai, Z. Fang *et al.*, Science **325**, 178 (2009).
[8] H. Zhang, C.-X. Liu, X.-L. Qi, X. Dai, Z. Fang, and S.-C. Zhang, Nat. Phys. **5**, 438 (2009).
[9] Y. Ando, J. Phys. Soc. Jpn. **82**, 102001 (2013).
[10] C. L. Kane and E. J. Mele, Phys. Rev. Lett. **95**, 146802 (2005).
[11] L. Fu, C. L. Kane, and E. J. Mele, Phys. Rev. Lett. **98**, 106803 (2007).
[12] D.-X. Qu, Y. S. Hor, J. Xiong, R. J. Cava, and N. P. Ong, Science **329**, 821 (2010).
[13] Y. Xia, D. Qian, D. Hsieh, L. Wray, A. Pal, H. Lin, A. Bansil, D. Grauer, Y. Hor, R. Cava *et al.*, Nat. Phys. **5**, 398 (2009).
[14] D. Hsieh, Y. Xia, D. Qian, L. Wray, J. Dil, F. Meier, J. Osterwalder, L. Patthey, J. Checkelsky, N. Ong *et al.*, Nature (London) **460**, 1101 (2009).
[15] T. Zhang, P. Cheng, X. Chen, J.-F. Jia, X. Ma, K. He, L. Wang, H. Zhang, X. Dai, Z. Fang, X. Xie, and Q.-K. Xue, Phys. Rev. Lett. **103**, 266803 (2009).
[16] S. K. Mishra, S. Satpathy, and O. Jepsen, J. Phys.: Condens. Matter **9**, 461 (1997).
[17] P. Larson, S. D. Mahanti, and M. G. Kanatzidis, Phys. Rev. B **61**, 8162 (2000).
[18] P. Larson, Phys. Rev. B **68**, 155121 (2003).
[19] M. Michiardi, I. Aguilera, M. Bianchi, V. E. de Carvalho, L. O. Ladeira, N. G. Teixeira, E. A. Soares, C. Friedrich, S. Blügel, and P. Hofmann, Phys. Rev. B **90**, 075105 (2014).
[20] G. A. Thomas, D. H. Rapkine, R. B. Van Dover, L. F. Mattheiss, W. A. Sunder, L. F. Schneemeyer, and J. V. Waszczak, Phys. Rev. B **46**, 1553 (1992).
[21] A. Dubroka, O. Caha, M. Hronček, P. Friš, M. Orlita, V. Holý, H. Steiner, G. Bauer, G. Springholz, and J. Humlíček, Phys. Rev. B **96**, 235202 (2017).
[22] Y.-Y. Li, G. Wang, X.-G. Zhu, M.-H. Liu, C. Ye, X. Chen, Y.-Y. Wang, K. He, L.-L. Wang, X.-C. Ma *et al.*, Adv. Mater. **22**, 4002 (2010).
[23] C. Chen, S. He, H. Weng, W. Zhang, L. Zhao, H. Liu, X. Jia, D. Mou, S. Liu, J. He *et al.*, Proc. Natl. Acad. Sci. USA **109**, 3694 (2012).
[24] J. Sánchez-Barriga, M. R. Scholz, E. Golias, E. Rienks, D. Marchenko, A. Varykhalov, L. V. Yashina, and O. Rader, Phys. Rev. B **90**, 195413 (2014).
[25] P.-Y. Chuang, S.-H. Su, C.-W. Chong, Y.-F. Chen, Y.-H. Chou, J.-C.-A. Huang, W.-C. Chen, C.-M. Cheng, K.-D. Tsuei, C.-H. Wang *et al.*, RSC Adv. **8**, 423 (2018).
[26] I. Mohelský, A. Dubroka, J. Wyzula, A. Slobodeniuk, G. Martinez, Y. Krupko, B.A. Piot, O. Caha, J. Humlíček, G. Bauer, G. Springholz, and M. Orlita, Phys. Rev. B **102**, 085201 (2020).
[27] R. S. Allgaier, Phys. Rev. **152**, 808 (1966).
[28] A. von Middendorff and G. Landwehr, Solid State Commun. **11**, 203 (1972).

[29] H. Köhler, Phys. Status Solidi B **74**, 591 (1976).

[30] A. Hashibon and C. Elsässer, Phys. Rev. B **84**, 144117 (2011).

[31] V. A. Kul'bachinskii, A. Y. Kaminskii, K. Kindo, Y. Narumi, K. Suga, P. Lostak, and P. Svanda, J. Exp. Theor. Phys. Lett. **73**, 352 (2001).

[32] J. Horák, J. Navrátil, and Z. Starý, J. Phys. Chem. Solids **53**, 1067 (1992).

[33] S. V. Dordevic, M. S. Wolf, N. Stojilovic, H. Lei, and C. Petrovic, J. Phys.: Condens. Matter **25**, 075501 (2013).

[34] T. Dong, R.-H. Yuan, Y.-G. Shi, and N.-L. Wang, Chin. Phys. Lett. **30**, 127801 (2013).

[35] S. Shigetomi and S. Mori, J. Phys. Soc. Jpn. **11**, 915 (1956).

[36] H.-W. Jeon, H.-P. Ha, D.-B. Hyun, and J.-D. Shim, J. Phys. Chem. Solids **52**, 579 (1991).

[37] H. Chi, W. Liu, K. Sun, X. Su, G. Wang, P. Lošt'ák, V. Kucek, Č. Drašar, and C. Uher, Phys. Rev. B **88**, 045202 (2013).

[38] G. Miller and C.-Y. Li, J. Phys. Chem. Solids **26**, 173 (1965).

[39] S. Biswas and R. Bhattacharya, Phys. Status Solidi B **151**, 193 (1989).

[40] V. A. Kulbachinskii, M. Inoue, M. Sasaki, H. Negishi, W. X. Gao, K. Takase, Y. Giman, P. Lostak, and J. Horak, Phys. Rev. B **50**, 16921 (1994).

[41] V. I. Fistul, *Heavily Doped Semiconductors*, Monographs in Semiconductor Physics (Springer, Berlin, 1969).

[42] T. Plecháček, J. Navrátil, and J. Horák, J. Solid State Chem. **165**, 35 (2002).

[43] J. R. Drabble, Proc. Phys. Soc. **72**, 380 (1958).

[44] H. Köhler, Phys. Status Solidi B **73**, 95 (1976).

[45] V. A. Kulbachinskii, Z. D. Kovalyuk, and M. N. Pyrlya, Phys. Status Solidi B **169**, 157 (1992).

[46] N. Abdullaev, S. Kakhramanov, T. Kerimova, K. Mustafazeva, and S. Nemov, Semiconductors **43**, 145 (1992).

[47] D. P. A. Holgado, K. Bolaños, S. de Castro, H. S. A. Monteiro, F. S. Pena, A. K. Okazaki, C. I. Fornari, P. H. O. Rappl, E. Abramof, D. A. W. Soares *et al.*, Appl. Phys. Lett. **117**, 102108 (2020).

[48] B. Schröder, A. von Middendorff, H. Köhler, and G. Landwehr, Phys. Status Solidi B **59**, 561 (1973).

[49] A. Kuzmenko, Rev. Sci. Instrum. **76**, 083108 (2005).

[50] W. Richter and C. R. Becker, Phys. Status Solidi B **84**, 619 (1977).

[51] E. D. Palik and J. K. Furdyna, Rep. Prog. Phys. **33**, 1193 (1970).

[52] H. Ehrenreich, J. Phys. Chem. Solids **2**, 131 (1957).

[53] I. Lang, Sov. Phys. Solid State **3**, 1871 (1962).

[54] Y. Ravich, Sov. Phys. Solid State **7**, 1466 (1965).

[55] I. Vurgaftman, J. R. Meyer, and L. R. Ram-Mohan, J. Appl. Phys. **89**, 5815 (2001).

[56] H. Yokoi, S. Takeyama, N. Miura, and G. Bauer, Phys. Rev. B **44**, 6519 (1991).

[57] J. P. Heremans, R. J. Cava, and N. Samarth, Nat. Rev. Mater. **2**, 17049 (2017).

[58] I. Witting, T. Chasapis, F. Ricci, M. Peters, N. Heinz, G. Hauter, and G. Snyder, Adv. Electron. Mater **5**, 1800904 (2019).

[59] T. Fang, X. Li, C. Hu, Q. Zhang, J. Yang, W. Zhang, X. Zhao, D. J. Singh, and T. Zhu, Adv. Funct. Mater. **29**, 1900677 (2019).

[60] I. Bejenari and V. Kantser, Phys. Rev. B **78**, 115322 (2008).

[61] I. Bejenari, V. Kantser, and A. A. Balandin, Phys. Rev. B **81**, 075316 (2010).

[62] T. Hofmann, P. Kühne, S. Schöche, J.-T. Chen, U. Forsberg, E. Janzén, N. B. Sedrine, C. Herzinger, J. A. Woollam, M. Schubert, NRMADL, Appl. Phys. Lett. **101**, 192102 (2012).

[63] S. Das Sarma, S. Adam, E. H. Hwang, and E. Rossi, Rev. Mod. Phys. **83**, 407 (2011).